Theor Chem Acc (2006) 115: 86–99
DOI 10.1007/s00214-005-0054-4

REGULAR ARTICLE

**Vassiliki-Alexandra Glezakou · Yongsheng Chen
John L. Fulton · Gregory K. Schenter · Liem X. Dang**

# Electronic structure, statistical mechanical simulations, and EXAFS spectroscopy of aqueous potassium

Received: 28 May 2005 / Accepted: 7 July 2005 / Published online: 23 December 2005


**Abstract** We investigate the solvation structure of aqueous potassium ions, using a combination of electronic structure calculations, statistical mechanical simulations with a derived polarizable empirical potential and experimental measurement of the extended X-ray absorption fine structure (EXAFS) spectra. The potassium K-edge (at 3,608 eV) EXAFS spectra were acquired on the bending magnet of sector 20 at the Advanced Photon Source, at ambient conditions and for the concentrations of 1 and 4 m KCl. We focus on the coordination distances and the degree of disorder of the first hydration shell as determined by electronic structure calculations, molecular dynamics simulations and experimental measurement. Finally, we characterize the changes of the structure in the first hydration shell with increasing temperature as predicted by molecular simulation.

**Keywords** EXAFS · Debye-Waller factor · Electronic structure

## 1 Introduction

Ion mediation in water is one of the classic problems encountered in many chemical processes. Water is the most common solvent either in the laboratory or in biological systems; therefore understanding the interaction of ions and water is of paramount importance. A number of theoretical [1–11] and experimental [12–14] studies have been conducted on the subject. Environmental control of ions [15], or biological processes of ion channel transport and protein binding [16] are some broad examples of such important chemical processes. As a result, there is an ongoing theoretical and experimental effort devoted to the understanding of ion solvation [17, 18]. $K^+$ in particular, plays a very important biological role in electrical signaling in the nervous system [19].

V.-A. Glezakou (✉) · Y. Chen · J.L. Fulton · G.K. Schenter · L.X. Dang
Chemical Sciences Division, Pacific Northwest National Laboratory, Richland, WA 99352, USA
E-mail: Vanda.Glezakou@pnl.gov

In this study, we address some fundamental issues of the structure of aqueous potassium and how it is affected by temperature, using a combination of theoretical and experimental methods. Although the structure of solvated ions is not as well-defined as in the case of crystals, one can still define an average structure, which can be quite characteristic of the ion and its immediate environment. Structural parameters can be calculated from experimental measurements, *ab initio* electronic structure calculations or numerical simulations such as molecular dynamics (MD). Figure 1 gives a qualitative picture of these structural parameters, $N_O$, coordination number of nearest neighbors, $\sigma^2$, Debye–Waller factor, which corresponds to the half-width of the peak in the radial distribution function (RDF), $g_{KO}(r)$, and $R_O$, which is the center of the peak. The broken line depicts the (ideal) Gaussian peak centered at $R_{O,G}$, which in general, can be more symmetric and narrower than the real peak. This center is shifted compared to the one obtained experimentally, or even from the MD simulations. The coordination number can be calculated by direct integration of this first peak:

$$N_O = \rho_0 \int_{r_1}^{r_2} 4\pi r^2 g_{KO}(r) \mathrm{d}r \quad (1)$$

where $r_1$, and $r_2$ are the integration limits.

The Debye–Waller factor is a quantity which can be extracted from electronic calculations of clusters, within the harmonic approximation. It is a measure of both the static disorder and thermal vibrations around the solvated species, and consequently, the average number of the solvent molecules interacting with the solute. It is directly related to the potential of the mean force from which diffusive reaction rates can be determined, and therefore an accurate evaluation of this quantity is important.

In this paper, we use molecular dynamics simulations, electronic structure calculations and extended X-ray absorption fine structure (EXAFS) spectroscopy to evaluate the immediate environment about the solvated $K^+$ ions. MD simulations using empirical potentials have been applied successfully in the analysis of chemical and physical properties

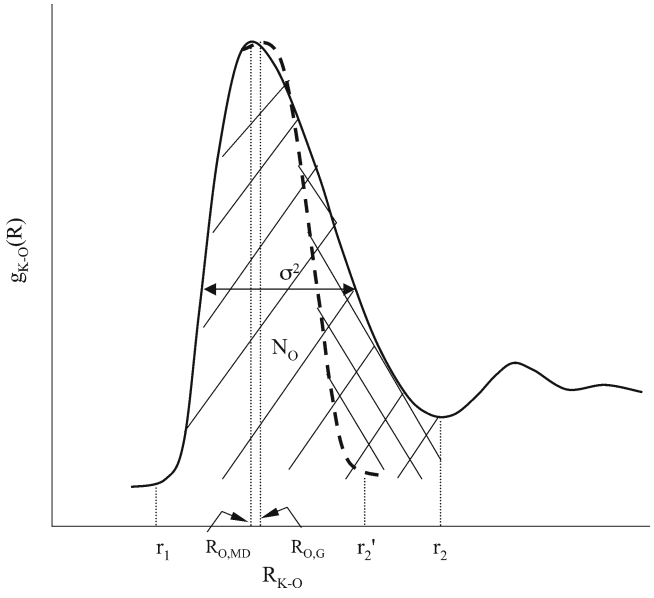


**Fig. 1** The fundamental quantities of ion solvation structure, coordination number $N_O$ (*area under curve*), Debye–Waller factor (half-width) $\sigma^2$, center of peak, $R_O$

of ions in solution [20]. An accurate description of a liquid interface remains a challenging problem, since it is highly dependent on the state of the solvent. The majority of water models focus on the properties of liquid water and are parametrized to reproduce the thermodynamic and structural properties under normal pressure and temperature. The main drawback is the lack of non-additive many-body interactions, which account for a significant part of the total interaction energy [2,5,21,22]. Polarizable potential models [23] include explicit treatment of the molecular polarizability of both the solute and the solvent, and the potential function parameters are optimized to reproduce aqueous cluster properties obtained from electronic structure calculations and experimental data, as well as experimental thermodynamic, structural and dynamical properties of bulk water. Such a model has charges at fixed distances such that they reproduce experimental gas-phase and *ab initio* results:

$$U_{\text{total}} = U_{\text{pair}} + U_{\text{pol}} \tag{2}$$

where the first term represents the pairwise additive potential and is the sum of the Lennard-Jones and Coulomb interactions, and the second term is the non-additive polarization energy [23]:

$$U_{\text{pair}} = \sum_i \sum_{j<i} \left[ 4\varepsilon \left( \left( \frac{\sigma_{ij}}{r_{ij}} \right)^{12} - \left( \frac{\sigma_{ij}}{r_{ij}} \right)^{6} \right) + \frac{q_i q_j}{r_{ij}} \right] \tag{2.1}$$

$$U_{\text{pol}} = -\sum_i \mu_i \cdot \mathbf{E}_i^0 - \frac{1}{2} \sum_j \sum_{i \neq j} \mu_i \cdot \mathbf{T}_{ij} \cdot \mu_j + \sum_i \frac{\mu_i \cdot \mu_i}{2\alpha_i} \tag{2.2}$$

where $r_{ij}$ is the distance between site $i$ and $j$, $q_i$ is the charge, $\sigma_{ij}$ and $\varepsilon_{ij}$ are the Lennard-Jones parameters, $\mathbf{E}_i^0$ is the electric field, $\mu_i$ the induced dipole moment and $\alpha_i$ the polarizability at site $i$ and $\mathbf{T}_{ij}$ is the dipole tensor. This model is used to generate the radial distribution functions that can then be combined with electronic structure calculations and compared to EXAFS spectral quantities.

Molecular orbital calculations are often employed on ion–water clusters to determine their structural or ligand exchange properties [24–27]. Systematic comparisons with crystallographic data reveal differences in the coordinative behavior between different ions, and the preferred coordination number for individual species. Although additional shells are usually required to fully mimic bulk aqueous conditions, cluster calculations still bear considerable relevance to the first hydration shell in solution, and can be used in conjunction with continuum representations of the surrounding solvent. We employ *ab initio* electronic structure calculations to determine the structures of $K^+[H_2O]_n^+$ clusters, where $n$=1–8. We apply the harmonic analysis for the evaluation of the Debye-Waller factors, which we combine with the RDF from molecular simulations to determine an 'average' value of the Debye–Waller factor for aqueous $K^+$.

Although $K^+$ is ubiquitous in aqueous systems, the experimental determination of its hydration structure is one of the most difficult challenges for the diffraction-based methods, such as neutron or X-ray diffraction, because the $K^+$-$H_2O$ length is nearly the same as that of $H_2O/H_2O$ interaction [18]. Neutron diffraction with isotopic substitution (NDIS) has the potential for separating the $K^+/H_2O$ and $H_2O/H_2O$ contribution as has been reported [28,29]. The difficulty with NDIS is that the scattering length difference (or contrast) of the two common K isotopes is relatively small, and the hydration shell appears to be highly disordered leading to interpenetration of the $g_{KO}(r)$ and $g_{KH}(r)$ [30]. The other common experimental method of EXAFS spectroscopy [31–34] has been widely used to characterize the structure of the first peak in $g(r)$ of solvated ions. The EXAFS signal quickly weakens with distance, and so only the immediate neighbors contribute to the spectrum. The major advantage of EXAFS over other scattering methods is that it is a highly specific probe about the central absorbing atom, and in the case of $K^+$, the $K^+/H_2O$ distance is completely decoupled from all $H_2O/H_2O$ distances.

In EXAFS, X-rays of appropriate energy are used to stimulate the excitation of a core electron of the ion, into a continuum state. The excited photoelectron is scattered by the neighboring atoms creating interference with the initial wavepacket and resulting in oscillations of the absorption spectrum. The Fourier transform of these oscillations produces a real-space distribution function, which can be decomposed into terms that allow the computation of various structural parameters [33]. The standard EXAFS relationship is:

$$\chi(k) = \sum_i \frac{N_i}{kR_i^2} F_i(k) \times \sin[2kR_i + \phi_i(k)] e^{-2\sigma_i^2 k^2} e^{-2R_i/\lambda}, \tag{3}$$

where $N_i$ is the number of the $i$th-shell neighbors at $R_i$ distance from the absorbing atom, $F_i$ is the backscattering amplitude, $\sigma_i^2$ is their mean-square displacement (Debye–Waller factor), $\phi_i(k)$ the photoelectron phase-shift, and $\lambda$ the mean-free path of the photoelectron. This last exponential term accounts for the inelastic scattering and damping of the EXAFS signal with distance. Only in the limit of low disorder does the Debye–Waller factor measured by EXAFS correspond to the peak width of the $g(r)$. The application of EXAFS to aqueous systems in which there is a high degree of disorder has recently been reviewed [34,35]. For highly disordered systems, the 'Gaussian approximation' in Eq. (2) can be extended with terms treating the nature of the disorder such as the anharmonicity in the pair potential.

With the wider availability of intense X-ray sources and consequent abundance of experimental data, a serious theoretical effort has been developed for the modeling and interpretation of EXAFS spectra. Codes like FEFF 8.0 [36] have been developed and used with considerable success for the direct simulation of EXAFS spectra, by evaluating the full range of scattering processes for large clusters of atoms. The accuracy of this analysis from the experimental data is 0.01–0.02 Å for distances, 20% for coordination numbers and about 15% for the Debye–Waller factors. Methods have been developed to generate EXAFS spectra from an MD simulation (MD-EXAFS) [37,38].

## 2 Computational details

### 2.1 Potential models and simulation methods

We employed the rigid-body polarizable water model of Dang and Chang [22] to describe the water–water intermolecular interaction. The functional form of the empirical potential includes a sum of Lennard–Jones Coulombic interaction and polarization term in order to account for many-body effects. This model describes reasonably well the structure and the thermodynamic properties of the bulk and the liquid/vapor interface of water. The polarizable potential parameters for the ion–water interactions were developed to reproduce the experimental solvation enthalpy and the structural properties of solvated ions in liquid water.

The MD simulations for this system consist of 550 water molecules and a $K^+$ ion in a cubic simulation cell with an average linear dimension of 25.5 Å per side. We carried out the simulations using the identical protocol as used in our earlier work on the calcium and strontium ions [37]. The simulations were carried out in an isobaric–isothermal (NPT) ensemble at 1 atm and 300, 350 and 400 K, with time steps for the heat bath coupling and pressure relaxation of 0.1 and 0.2 ps, respectively [39]. In all MD simulations, a step of 2 fs was used. After an energy minimization to relax the initial coordinates, the simulation was carried out to 300 ps to equilibrate the system, followed by at least 500 ps of data collection for analysis. The MD-EXAFS spectra were averaged over the 500 configurations with each configuration separated by 100 timesteps. The relation between the details of intermolecular potential and a prediction of EXAFS spectra builds on previously published work in MD-EXAFS [37, 38] where the ensemble of molecular configurations generated by the intermolecular potential is used in electron scattering analysis. In the present work we employ an updated version of the efficient algorithm for evaluating the electron scattering series by Rehr et al. [40], in its most current implementation in the code FEFF8.2 [36].

### 2.2 Electronic structure

There have been several theoretical [1,6–10,41–47] and experimental [13,14,48] studies on ion–water clusters, most of them focusing on the evaluation of binding energies. *Ab initio* calculations on bigger clusters were and still are quite challenging, especially for correlated methods. One is forced to use incomplete basis sets and lower level theories, especially when examining larger systems. Experimental data from neutron scattering or X-ray spectroscopies, are particularly valuable for benchmarking purposes, although systematic errors can still be disguised. Systematic studies and approximations, taking into account the particular system, are always the best approach.

The choice of the basis sets is very important in the case of these systems. It has been found that extended basis sets augmented with diffuse functions on the oxygen atoms are very important in describing interactions with water [8]. In the case of the alkali metals and earths, the formal charge of the system (+1 or +2) implies a $(n-1)$ occupied valence shell. It has been shown that for these elements, core-valence correlation is particularly important in calculating reliable structural [8,49] and thermochemical properties. Model *ab initio* calculations used to parametrize semiempirical force fields for Ca-protein simulations have suffered from the use of inadequate Ca basis sets. In the case of $Ca^{2+}$, core/valence correlation and diffuse functions are very important in order for geometries to agree within 2% [49]. For the same reason, if effective core potentials are used the $(n-1)$ shell should be explicitly treated and not included in the pseudopotential, and for post-Hartree–Fock treatments, the core/valence electrons and orbitals should be included in the active space, instead of being part of the frozen core. In the case of $K^+$, as well as $Cs^+$, and $Ru^+$, some water bonding orbitals are below some of the core/valence orbitals of the metal, and therefore they are not treated equally. Inclusion of the core electrons in the correlation treatment has minor effect of about 4% on binding energies [47], and ~0.05 Å on the bond lengths [8].

We used aug-cc-pVDZ [49,50] basis for water and the core/valence tailored basis of double zeta quality extended with one set of $(s, p, d)$ polarization functions [8,51] for K, which will be referred as aug-CV-pVDZ. Use of aug-cc-pVDZ quality basis sets has been shown to affect binding energies by less than 2% [8], and bigger basis would make computations too expensive for the bigger clusters at the correlated level. The calculations were performed with the GAMESS-US suite of codes [52]. Geometry optimizations and harmonic analysis were performed at the MP2 level of

theory. The frequencies were calculated by double numerical differences of the analytic gradients, and were subsequently scaled by the appropriate scaling factor [53].

## 2.3 Experimental

Potassium $K$-edge (3608.4 eV) EXAFS spectra were collected on a bending magnet beamline (Sector 20) run by the Pacific Northwest Consortium – Collaborative Access Team (PNC-CAT) at the Advanced Photon Source (APS), Argonne National Laboratory. Three single 20-min scans were co-added to obtain high-quality transmission spectra. The arrangement of the X-ray optics to achieve a high level of harmonic rejection and the methods for energy calibration have been previously described [54]. With this method, the first inflection in the spectra (transmission) for the 1 m aqueous KCl solution was located at 3610.5 eV after energy calibration to the Ti(0) $K$-edge (4966). Acquisition of EXAFS spectra at the potassium $K$-edge is a challenging problem because the strong X-ray absorption by the windows and the solution severely limits the transmission. The liquid sample holder used in these studies has been previously described for studies of $Ca^{2+}$ solutions [54]. In this method a very thin liquid layer is contained between two pieces of thin prolene film (isotactic polypropylene) that are stretched over a "U"-shaped Kapton spacer that defines the pathlength. The solution pathlength was set at 75 $\mu$m and the solution was contained between two, 4 $\mu$m thick prolene windows. Spectra that were acquired at different path lengths and at different concentrations were identical demonstrating that absorption effects did not distort the $\chi(k)$ data. In general, the absorption edge height $\Delta\mu x$, for these transmission measurements was below 1.5 in all cases as required to eliminate X-ray leakage effects.

During the fitting process the weighting of the potassium $\chi(k)$ data was increased to $k^3$ to better capture the information on K–O structure contained in the region from $6 < k < 10\,\text{Å}^{-1}$. The data were windowed between $2.0 < k < 9.5\,\text{Å}^{-1}$ using a Hanning window with $\mathrm{d}k = 1.0\,\text{Å}^{-1}$. The fits were applied to both the real and imaginary parts of $\tilde{\chi}(R)$ in the region of $1.0 < R < 4.0$ Å. The uncertainties associated with the fit correspond to an increase in the misfit (defined by a scaled sum of squares, $\chi^2_{\text{FEFFIT}}$) between the data and the best-fit model by an amount of $1/\nu$, where $\nu$ is the degrees of freedom in the fit. The values calculated by FEFF8 for the *muffin-tin* radii of 2.01, 1.09, and 0.85 Å for K, O, and H, respectively, were used without modification. In general, the contribution from second and higher hydration shells has negligible effect on the measured or simulated $\chi(k)$ spectra because the distances and the disorder are too large. For the experimental spectrum, including single scattering paths for K–H did not improve the quality of the fits, nor did adding triangular scattering paths describing the K–O–H and K–O–O paths.

In order to estimate the core–hole factor, $S_0^2$, we used the coordination numbers and distances from crystallographic data to fit the solid KCl reference compound. The KCl was finely ground into an inert hydrocarbon grease and spread in a thin layer for the transmission measurement. The $S_0^2$ value was then found to be 0.98 for KCl, a similar value as that reported for RbCl [55]. Uncertainties in the experimental estimate of $S_0^2$ lead to an error of approximately 20% in the reported coordination numbers.

For $K^+$ aqueous systems, in which there is a higher degree of disorder in the first solvation shell, the EXAFS oscillations are relatively weak, and contributions from weak multi-electron excitations [56–58] represent a larger proportion of the total absorption intensity. For $K^+$, there are several multi-electron excitations that are removed using methods similar to those previously described [54]. These excitations occur at $k = 2.6$, 3.4 and $9.6\,\text{Å}^{-1}$ corresponding to the $KM_{II,III}$, $KM_I$ and $KL_{II,III}$ transitions, respectively. The same series of excitations with similar edge-step magnitudes are clearly evident in atomic K vapor [59] and Ar gas. Our strategy for efficient removal is to first fit the general multi-electron background features of Ar with arctan+slope change functions ($KM_{II,III}$, $KL_{II,III}$) and with an arctan function ($KM_I$). The energy position of these multi-electron edges are then rescaled to potassium (K) energies using the ($Z$+1) model for the onset of the multi-electron edges. The ($Z$+1) rule, states that the energy required to eject the second electron after creation of a core–hole vacancy is equal to the binding energy of that electron for the next higher element [60]. The fitting of the $K^+$ /$H_2O$ structural parameters was compared both with and without removal of the multi-electron features.

## 2.4 MD-EXAFS

Several steps are required to convert the average molecular configurational information from the MD simulation into an EXAFS spectrum. In standard EXAFS analysis, the fine structure factor is defined by:

$$\chi(E) = \frac{\mu(E) - \mu_0(E)}{\Delta\mu_0(E_0)}, \tag{4}$$

where $\mu(E)$ is the absorption coefficient as a function of X-ray energy $E$, $\mu_0(E)$ is the background absorption coefficient and $\Delta\mu_0(E_0)$ is the jump in the absorption background at the absorption edge, $E_0$. Given a set of neighboring atoms located at positions $\mathbf{r}_i$ relative to the photoelectron source located at $\mathbf{r}_0$, with $R_i = |\mathbf{r}_i - \mathbf{r}_0|$, the EXAFS signal in $k$-space is described by:

$$\chi(k) = \sum_i S_0^2 \frac{F_i(k)}{kR_i^2} \mathrm{e}^{-2R_i/\lambda} \sin\left[2kR_i + \phi_i(k)\right] \tag{5}$$

where the photoelectron wave-vector, $k$, is related to the X-ray energy by $E = E_0 + (\hbar^2 k^2)/2m_e$. The effective backscattering amplitude, $F_i(k)$ and the phase shift, $\phi_i(k)$ are determined from multiple scattering analyses. The mean free path, $\lambda$, accounts for inelastic scattering effects, while the amplitude reduction factor, $S_0^2$, accounts for many body effects in a single particle theory. The $k^2$-weighted $\chi(k)$ were

Fourier-transformed to obtain radial structure functions. In the current analysis the potassium $K$-edge excitation was probed.

A maximum path length of 5.5 Å was used in the sampling of the configurations used in the MD simulations. Increasing this to 6.0 Å did not result in any significant modifications of the calculated spectra. The advanced features of the current version of FEFF8.20 were employed, taking advantage of self-consistent potentials. FEFF's automated self-consistent potential calculation with a radius of 3.1 Å for the full multiple scattering during the self-consistency loop was employed. The average EXAFS spectrum from the simulation was obtained from a configurationally average:

$$\bar{\chi}(k) = \frac{\bar{\mu}(E) - \mu_0(E)}{\Delta\mu_0(E_0)}, \tag{6}$$

where Eq. (6) represents a configurationally average of Eq. (4). The configurationally average is often fitted to the expression:

$$\bar{\chi}(k) = \sum_i N_i S_o^2 \frac{\bar{F}_i(k)}{k\bar{R}_i^2} \mathrm{e}^{-2\bar{R}_i/\lambda - 2k^2\sigma_i^2} \times \sin\left[2k\bar{R}_i + \bar{\phi}_i(k) - \frac{4}{3}C_{3,i}k^3\right]. \tag{7}$$

In this expression, $\bar{F}_i(k)$ is often estimated from a single characteristic configuration and assumed to have insignificant fluctuations with configuration. The Debye–Waller factor, $\sigma^2$, and the third cumulant, $C_3$, reflect the structural disorder of the system.

To obtain a real space representation of the EXAFS spectra, we calculated the Fourier transform of the structure factor as implemented in the FEFFIT package [32]. Equation (6) is thus transformed to:

$$\tilde{\chi}(R) = \frac{1}{\sqrt{2\pi}} \int_0^\infty k^2 \bar{\chi}(k) W(k) \mathrm{e}^{i2kR} \mathrm{d}k, \tag{8}$$

where $W(k)$ is a Hanning window.[1]

Experimental and simulated spectra were transformed in an identical manner for direct comparison. $\tilde{\chi}(R)$ reduces to a series of peaks centered at the atomic distances $R_i$, in the limit that $F_i(k)$ and $\phi_i(k)$ do not depend on $k$. Aside from the distortion due to the electron scattering and phase shift described in Eq. (4), $\tilde{\chi}(R)$ is a direct measurement of the radial probability, $4\pi R^2 g(R)$ in the region of the first solvation shell.

[1] $W(k) = \sin^2\left(\frac{\pi(k - k_{\min} + \Delta k/2)}{2\Delta k}\right), k_{\min} - \frac{\Delta k}{2} \le k < k_{\min}$

$W(k) = 2.0, k_{\min} + \frac{\Delta k}{2} \le k \le k_{\max} - \frac{\Delta k}{2}$

and $W(k) = \cos^2\left(\frac{\pi\left(k - k_{\max} + \frac{\Delta k}{2}\right)}{2\Delta k}\right), k_{\max} - \frac{\Delta k}{2} < k \le k_{\max} + \frac{\Delta k}{2}$. We set $k_{\min} = 4\,\text{Å}^{-1}$, $\Delta k = 1\,\text{Å}^{-1}$ and $k_{\max} = 9.5\,\text{Å}^{-1}$

## 3 Results and discussion

### 3.1 MD simulations

The optimized ion–water potential parameters (i.e. Lennard–Jones) were obtained by carrying out a series of MD simulations. During the simulation, the ion-water Lennard–Jones parameters were modified until the calculated solvation enthalpies and hydration numbers reproduced the experimental measurements. The final potential parameters for the $K^+$ ion and for the water model are listed in Table 1.

In Fig. 2, we show the ion–water interaction energy as a function of the separation distance. The minimum energies as well as the ion–water distances were in good agreement with the results obtained from ab initio molecular orbital theory calculations [8]. The calculated RDF for the $K^+$–$H_2O$ system is included in Fig. 3, while Fig. 4 shows the first RDF peak, $g_{KO}(r)$ at three different temperatures. The following observations are in order:

- The RDFs are quite narrow with well-defined first and second hydration shells, implying a strong interaction among these species. The peaks tend to become slightly broader as the temperature increases, indicative of the increased disorder of the system with temperature.

**Table 1** Potential parameters for $K^+$ and $H_2O$ used in the molecular dynamics (MD) simulations

| Molecule | Atom | $\sigma$(Å) | $\varepsilon$(kcal/mol) | $q(e)$ | $\alpha$(Å$^3$) |
|---|---|---|---|---|---|
| $H_2O$ | H | 0.000 | 0.0000 | 0.5190 | 0.000 |
| | O | 3.234 | 0.1825 | 0.0000 | 0.000 |
| | M | 0.000 | 0.0000 | −1.0380 | 1.444 |
| $K^+$ | K | 3.047 | 0.1000 | 1.0000 | 0.830 |

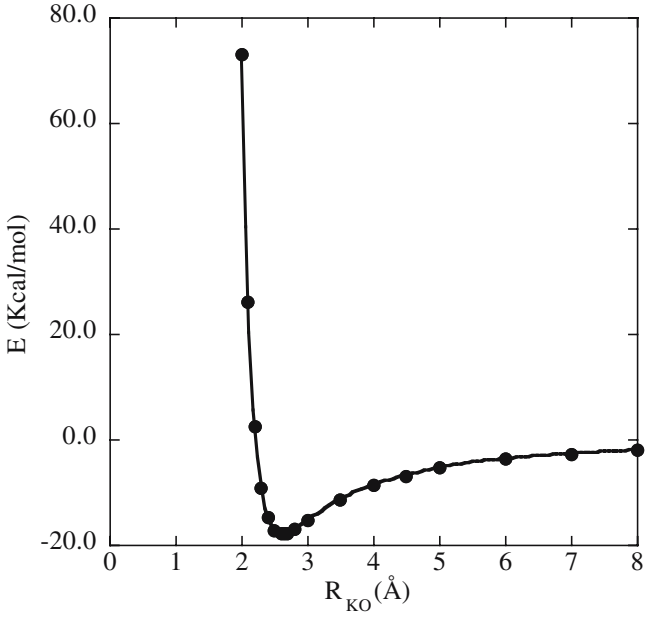


**Fig. 2** $K^+$–$H_2O$ interaction energy. Energies are in kcal/mol, and distances $R_{KO}$ in Å

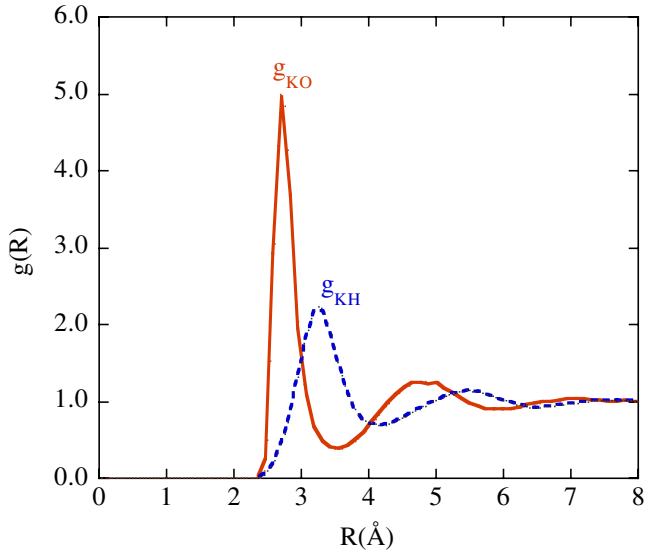


**Fig. 3** Radial distribution functions for K–O and K–H interactions. Distances are in Å

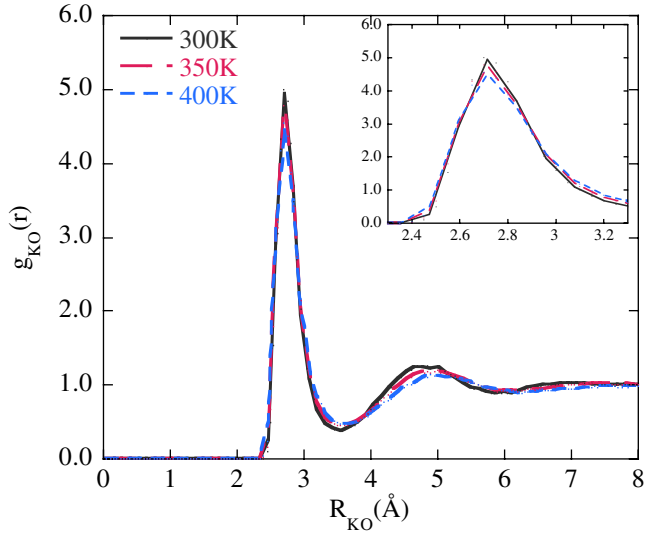


**Fig. 4** Radial distribution function for K–O for $T = 300$, 350 and 400 K. Distances are in Å

- The coordination number obtained by integration of the first peak in the RDF, out to its first minimum are 6.8, which is in excellent agreement with 7, the result from recent MD simulation and experimental measurements [48].
- The hydration enthalpies, calculated using a method described previously are also in good agreement with the experimental values [48].
- The K–O distance and coordination number from the MD simulation of *2.725* Å and 6.8 respectively, are in good agreement with recent *ab initio* dynamics simulations where values of 2.80 Å and 6.0–6.8 are reported [62,63]. Qualitatively, the width of the first peak in $g_{KO}(r)$ is somewhat narrower for the MD simulation.

**Table 2** Structural and thermodynamic properties of $K^+$ in water at 300 K

| Parameters | MD[a] | MD, Exp |
|---|---|---|
| $R_{KO}$(Å) | 2.725 | 2.6–2.8[b] |
| $R_{KH}$(Å) | 3.25 | 3.30[b] |
| $N$ | 6.8 | 5–8 |
| $\Delta H_{sol}$(kcal/mol) | −71.0±5.0 | −76.0[c] |

[a]This work.
[b]Ref. [48]
[c]Ref. [12]

The simulated peak positions, coordination numbers and hydration enthalpies are summarized in Table 2, along with the available experimental data. The peak position rather than the peak center reported in Table 2 from the MD simulation corresponds to the peak maximum in $g_{KO}(r)$ (see Fig. 1). Having thus first established the good agreement between simulation results and both the experimental and *ab initio* data, we will use the simulated hydration structure to compute the MD-EXAFS spectra for dilute $K^+$ in solution (Sect. 3.3).

## 3.2 Electronic structure and fitting

We performed electronic structure calculations on $K^+(H_2O)_n$ clusters where $n$=1–8, at the MP2/aug-CV-PVDZ level of theory. All structures were optimized and the harmonic frequencies were obtained by numerical difference of the analytic gradients at the same level. The harmonic frequencies were subsequently scaled by a factor of 0.96 [53]. Table 3 displays the energies and K–O distances for these clusters. The computations were done without any symmetry to allow for complete relaxation of the water molecules. In the table, we

**Table 3** MP2/aug-CV-pVDZ Energies (in atomic units), bond lengths (in Å)

| n | Symmetry[a] | E | R(K–O) |
|---|---|---|---|
| 1 | $C_{2v}$ | −675.4572273 | 2.647 |
| 2 | $D_{2d}$ | −751.7426615 | 2.681 |
| 3 | $C_3$ | −828.0252052 | 2.697 |
| 4 | '$T_d$'[b] | −904.3052021 | 2.713 |
| | '$C_{3v}$'[b] | −904.3089223 | 2.787(3),2.711 |
| | '$C_{4v}$' | −904.3104792 | 2.815 |
| 5 | '$C_{4v}$' | −980.5928387 | 2.855(4),2.708 |
| 6 | '$T_h$'[b] | −1056.8602807 | 2.756 |
| | '$S_6$' | −1056.8721626 | 2.831 |
| 7 | $C_1$[b] | −1133.1550847 | 2.901(4),2.840(3) |
| 8 | '$D_{4h}$'[b] | −1209.4375688 | 2.917 |

[a]Optimizations were performed without any symmetry to allow for complete relaxation of the waters, the symmetry labels thus correspond to an approximate orientation of the water molecules around the metal center. Quotes around the point groups mean that only O are considered in assigning the symmetry group. Only clusters with n water molecules in their first solvation shell are listed
[b]First or higher order saddle points at this level of theory, with very small imaginary frequencies
[c]In parentheses, number of equal bond distances

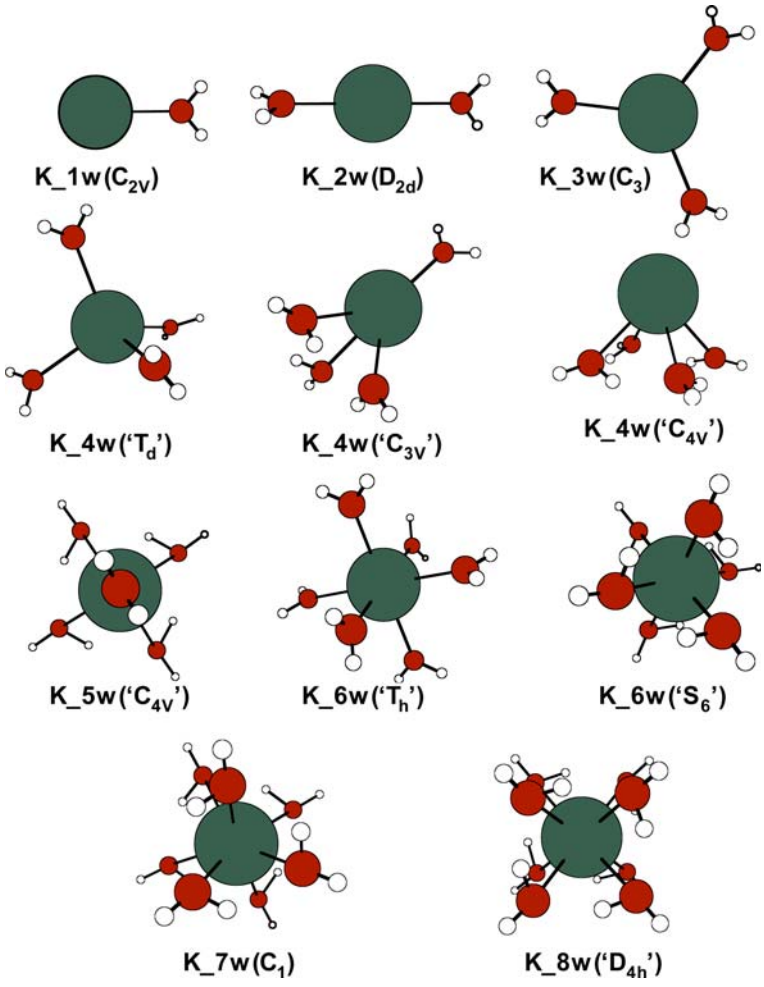


**Fig. 5** $K^+ (H_2O)_n$, $n = 1, 8$ clusters, MP2/aug-CV-pVDZ equilibrium structures. All structures optimized in $C_1$. When *in quotes*, symmetries take into account only the oxygen atoms

characterize them according to the local, approximate symmetry of the O atoms around the central atom. Bond lengths are quite sensitive to the orientation and number of the waters around the central atom. For example, the cluster with $n$=7 has two different groups of bond lengths. As is often the case with such systems, more than one quasi-degenerate minima exist for the same number of waters. Figure 5 displays the different clusters.

The disorder contributing to the Debye–Waller factor can be considered as the result of two sources, the configurational disorder and the vibrational disorder. The cluster studies are used to determine the latter, along with the universal curve relating the vibrational contribution to the Debye–Waller factor (Fig. 6). The configurational disorder is determined from the molecular dynamics simulation.

Within the harmonic approximation, there is a well-defined relationship between the harmonic displacements and the Debye–Waller factors:

$$\sigma^2 = \sum_i \left(\frac{\partial R_i}{\partial z_i}\right)^2 \frac{k_B T}{M\omega_i^2} \tag{9}$$

where $\omega_i$ is the harmonic frequency $i$, $M$ is the reduced mass and $Z_i$ is the normal coordinate $i$. For the K–O interactions, the symmetric and asymmetric stretches are the ones that have the main contributions. The Debye–Waller factors were also corrected for quantum effects according to the equation:

$$\sigma_{qe}^2 = \sum_i \left(\frac{\partial R_i}{\partial z_i}\right)^2 \frac{k_B T}{M\omega_i^2} w_i^{qe}, \tag{10}$$

where $w_i^{qe}$ is the scaling factor:

$$w_i^{qe} = \frac{\frac{\hbar\omega_i}{k_B T}}{2\tanh\left(\frac{\hbar\omega_i}{2k_B T}\right)}. \tag{11}$$

We applied a novel approach in which we combine the results from these calculations with MD simulations. The configurational disorder is thus convoluted with the vibrational disorder in order to obtain our best estimate of the total Debye–Waller factor, see Eq. (12).

The Debye–Waller factors obtained from the cluster calculations, were fitted to a logarithmic function over the range

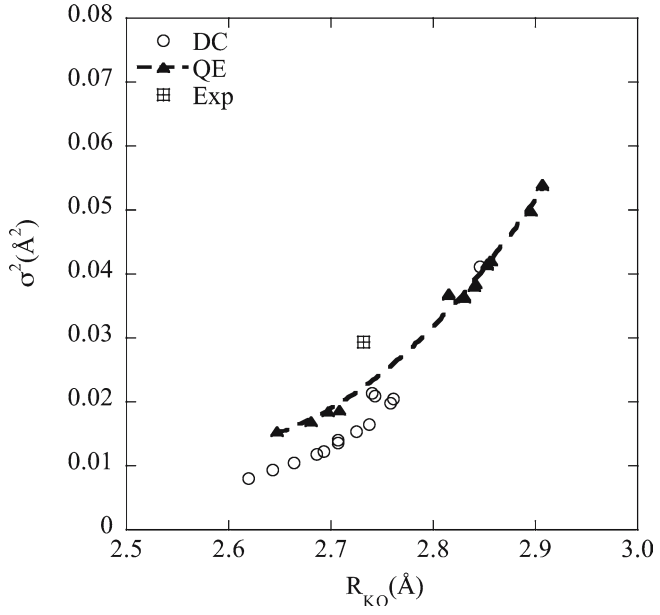


**Fig. 6** Debye–Waller factors from molecular dynamics (MD) simulation (DC, Dang–Chang potential) and *ab initio*, quantum-corrected calculations. Experimental values from EXAFS. All at 300 K

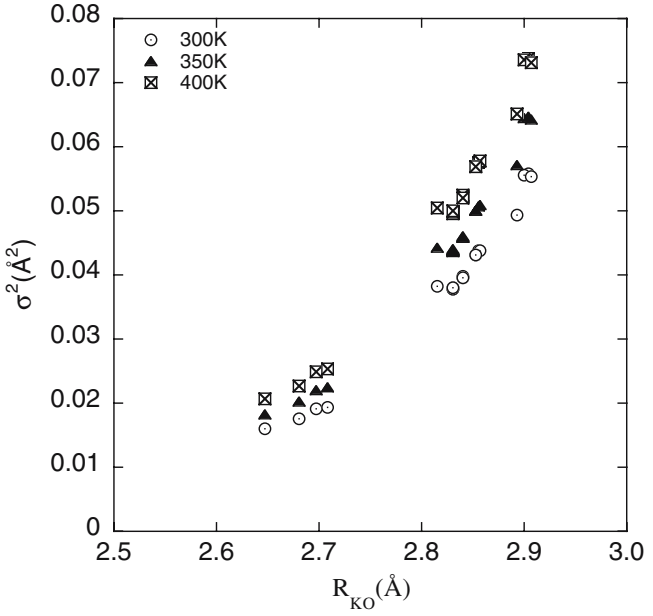


**Fig. 7** Debye–Waller factors from ab initio calculation at three different temperatures

of K–O distances of the first peak of $g_{KO}(r)$, which indicates the interaction within the first hydration shell. In the next step, we combined the *ab initio* results with the simulations in order to obtain an 'corrected' value for the Debye–Waller factor ('Direct evaluation', Table 4), which integrates the cluster approach with the continuum picture from the molecular simulations. For this purpose, we weighted the Debye–Waller factors by the MD-derived $g_{KO}(r)$:

$$\left\langle \frac{1}{\sigma^2} \right\rangle = \frac{\int_{r_1}^{r_2} \mathrm{d}r 4\pi r^2 g_{KO}(r) \exp(-\ln \sigma_f^2(r))}{\int_{r_1}^{r_2} \mathrm{d}r 4\pi r^2 g_{KO}(r)}. \quad (12)$$

The integration limits are taken to be the cutoffs for the first peak of the radial distribution function, $g_{KO}(r)$. This process was repeated for the three temperatures of 300, 350 and 400 K (Fig. 7) that the simulations were run.

Figure 6 compares the Debye–Waller factors calculated from the MD simulation with the polarizable model (Dang-Chang), and from electronic structure calculations on small clusters. The simulation underestimates the Debye–Waller factors.

The Debye–Waller factors can also be calculated through a Gaussian fit of the first peak, $g_{KO}(r)$:

$$\rho_0 4\pi r^2 g_{KO}(r) \approx \frac{N_O}{\sqrt{2\pi\sigma^2}} \mathrm{e}^{-\frac{(r-R_0)^2}{2\sigma^2}}. \quad (13)$$

From this fit, the number of nearest neighbors, coordination number $N_O$, and the center of the peak $R_O$ can be determined.

The number of nearest neighbors can also be calculated by direct integration over the first peak as defined from Eq. (1). The results are listed in Table 4. We find that the 'corrected' value of 0.0276 Å$^2$ is in good agreement with the experimental value of 0.0293 Å$^2$ reported in Sect. 3.3, and it is somewhat larger than the MD simulation value of 0.0221 Å$^2$.

**Table 4** Calculated values of Debye–Waller factors ($\sigma^2$), first shell coordination numbers ($N_O$), and $g_{KO}(r)$ maxima with temperature dependence

| T(K) | $\rho_0$(Å$^{-3}$) | Direct evaluation[a] | | Gaussian fit[b] | | |
|---|---|---|---|---|---|---|
| | | $N_O$ | $\sigma^2$(Å$^2$) | $N_O$ | $\sigma^2$(Å$^2$) | $R_0$(Å) |
| 300 | 0.03328 | 6.6 | 0.0276 | 5.7 | 0.0221 | 2.770 |
| 350 | 0.03161 | 6.6 | 0.0319 | 5.6 | 0.0263 | 2.777 |
| 400 | 0.02948 | 6.5 | 0.0365 | 5.3 | 0.0300 | 2.782 |

[a] $N_O$ was calculated by direct integration of the $g(r)$ corresponding to the K–O interaction (Eq. (1)), and the Debye–Waller factors according to the scheme described in the paper, Eq. (12)

[b] $N_O$, $\sigma^2$, and $R_O$ were computed as parameters of a Gaussian fit of the corresponding $g(r)$

## 3.3 MD-EXAFS and experiment

Five hundred statistically independent configurations out of 550 water molecules and one $K^+$ ion from the molecular dynamics simulations were taken into account for the MD-EXAFS analysis. For each configuration, a cluster of the 40 closest water molecules to the photoelectron source ($K^+$) were extracted from the configuration to form an input for electron multiple scattering analysis. This forms a cluster surrounding the $K^+$ ion with a radius of approximately 6 Å containing the first and second solvation shells. The radial distribution function resulting from the ensemble of clusters faithfully reproduces the structure of the ion–water RDF (radial distribution function) obtained from the bulk simulation. When more molecules were included in the configuration averaged evaluation of the EXAFS signal, no significant

effect was observed. This is due to the fact that configurationally disorder in the second and higher solvation shells dampens their direct distribution to the EXAFS signal. The indirect influence of the bulk waters on the structure of the first two solvation shells is fully taken into account.

Figure 8 displays the resulting $|\tilde{\chi}(R)|$ plots at three different temperatures, 300, 350, and 400 K. As in the case of the corresponding quantity $g(r)$ from the MD simulations, the same trend is observed: the peak heights are reduced as the temperature increases, indicating a higher disorder and lower coordination number.

In Fig. 9, the $k^2$-weighted $\chi(k)$ experimental data from 1.0 m KCl at 300 K is compared to the MD-EXAFS spectrum generated from the simulation. There is an overall excellent agreement for the frequency and fair agreement for the amplitude of the oscillations over the full $k$ range from 2 to about 9.5 Å$^{-1}$. The matching of the frequency of the oscillation means that the K–O distances are nearly the same between the experiment and the simulation. At $k = 9.6$ Å$^{-1}$, there is an artifact in the experimental data due to the $KL_{II,III}$ multi-electron edge that somewhat distorts the background function in this region. The corresponding $\tilde{\chi}(R)$ plots derived from the experimental measurements are shown in Fig. 10, together with the computed generated ensemble (MD-EXAFS). The $\tilde{\chi}(R)$ was generated by Fourier transform of the $k^2\chi(k)$ data, and they represent the partial pair distribution functions convoluted with the photoelectron scattering functions from Eq. (3). Again, there is remarkably good agreement in the radial structures of the experimental and simulated data. It is important to realize that the $\tilde{\chi}(R)$ are not exact representations of the $g_{KO}(r)$ [35]. The K–O phase shift function, $\phi_{KO}(k)$ in Eq. (3) alters the phase of the scattered photoelectron leading to significant broadening and an $R$-shift of the K–O peak in Fourier transformed $k^2\chi(k)$ data. However, $\phi_{KO}(k)$ is recovered exactly by FEFF8.2 so that the fitted parameters, as will be described later, provide a very close approximation to the first peak in $g_{KO}(r)$.

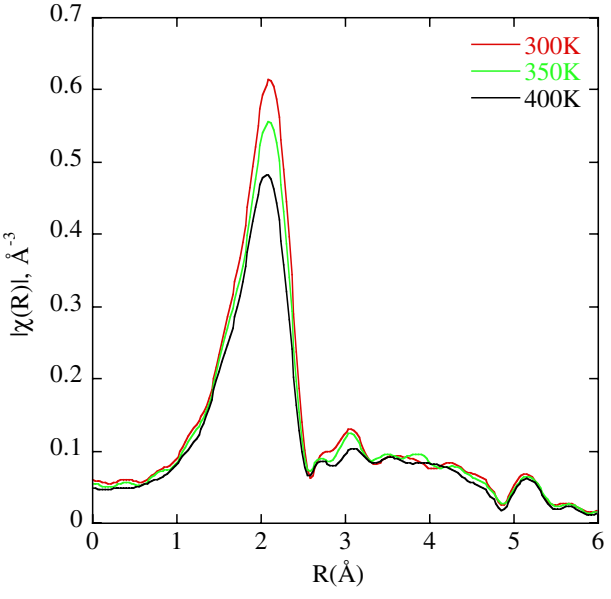


**Fig. 8** The $K^+$–$H_2O|\tilde{\chi}(r)|$ plot from the Fourier transformed $k^2\chi(k)$ MD-EXAFS data, at 300, 350 and 400 K

Figures 11, 12, 13 and 14 independently compare the $k^2\chi(k)$ and $\tilde{\chi}(R)$ spectra from the experiment and the MD simulation with their respective fits to the theoretical standards using the EXAFS Eq. (7). The solid lines represent the experimental data and the dashed lines are the EXAFS fits with parameters as reported in Table 5. In general, the quality of the fit to both the magnitude and the imaginary parts of $\tilde{\chi}(R)$ are excellent for the experimental and simulated spectra. Figure 11 also shows the experimental spectrum that has been corrected for the multi-electron edges as described above. Notably, the strong $KL_{II,III}$ feature at 9.6 Å$^{-1}$ is removed. In addition, removal of the relatively strong $KM_{II,III}$ feature at 2.6 Å$^{-1}$ results in attenuation of the oscillations between $k = 1.5$ and 3.0 Å$^{-1}$.

The structural parameters for the hydrated $K^+$ are summarized in Table 5. They have been extracted from experimental and simulated data by fitting to the FEFF8.2 theoretical standards. For the MD simulation, two methods of deriving the structural parameters are reported. In the first, an ensemble of different configurations is used to generate an average EXAFS spectrum from the simulation. This MD-EXAFS spectrum is then treated in a fashion identical to the experimental data to recover the structural parameters. This provides a very powerful method to identify the key differences between the simulations and the experimental structure. The second method of deriving the structural parameters from the MD simulation is a standard analysis of the peaks in the $g_{KO}(r)$ and $g_{KH}(r)$. The experimental data in Table 5 were evaluated after correction of the multi-electron features. Depending upon the position of the multi-electron edges with respect to important parts of the EXAFS oscillation, corrected spectra can improve the quality of the fits to the experimental parameters [63]. We find that in the case of $K^+$, removing the multi-electron features has only a minor effect on the fitted parameters primarily because these features are mostly outside the range of the important EXAFS oscillations.

The K–O distance from the experimental spectrum of 2.732 Å is in excellent agreement with both the MD-EXAFS value of 2.72 Å and that from the Gaussian fit to the RDF of 2.770 Å. On the other hand, the Debye–Waller factor, $\sigma^2$, is considerably larger for the experiment than that for the simulation. This trend is similar to what was observed for $Ca^{2+}$, where the amount of disorder in the $Ca^{2+}$–O interaction from the simulation was much less than for the experiment [37]. Literature values for the experimentally derived $K^+$ structural parameters are very limited primarily because the $K^+/H_2O$ distances from the X-ray diffraction are difficult to separate from the $H_2O/H_2O$ scattering contribution. For NDIS, the K–O distance overlaps with the K–H distance, so separate distances have not been obtained. All of the scattering methods provide $K^+/H_2O$ distances bounded by a general range from 2.6 to 2.95 Å$^{-1}$. The $K^+$–O distances from our

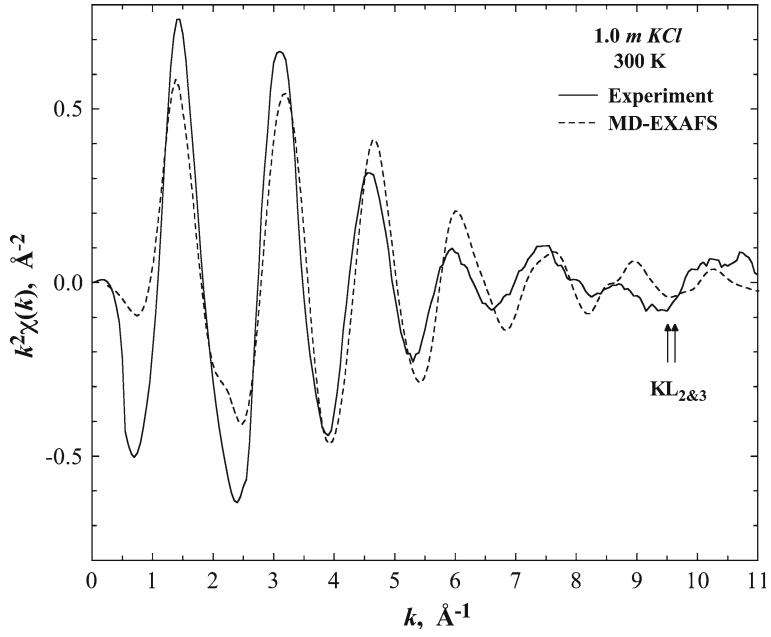


**Fig. 9** Potassium EXAFS $k^2$-weighted $\chi(k)$ plots for an aqueous 1.0 m KCl solution at 300 K. The *solid line* is the experimental data and the *dashed line* is the MD-XAFS. The experimental spectrum was acquired in transmission mode and is uncorrected for multi-electron edges. The $KL_{\mathrm{II,III}}$ multielectron edge for the experimental data is indicated

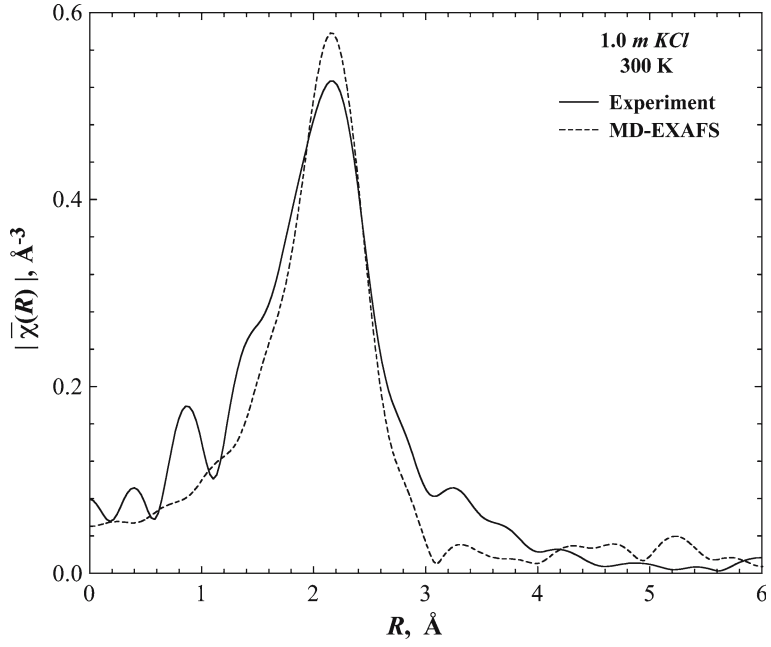


**Fig. 10** The $|\tilde{\chi}(R)|$ plots corresponding to the Fourier transformed $k^2\chi(k)$ shown in Fig. 9. The *solid line* shows the experimental data and the *dashed line* show MD-EXAFS data. The distances have not been corrected for phase shifts. The unphysical peak at 0.9 Å is an artifact of the multi-electron excitations

EXAFS values reported here represent one of the most accurate experimental measurements of the K–O distance.

Finally, we examine results for the water coordination number in the first solvation shell about $K^+$. The EXAFS experimental value of 6.1 with an uncertainty of about $\pm 1.3$ (uncertainty associated to the estimate of $S_0^2$) seems to be in agreement with the water coordination number of 6.8 from the integrated $g(r)$, and with 5.3 that has been reported from NDIS measurements [28]. However, when comparing EXAFS-derived coordination numbers for these more disordered systems to values from methods based upon the full $g(r)$, it is important to account for the short range sensitivity of EXAFS technique, as illustrated schematically in Fig. 1. This aspect is demonstrated by the fact that the coordination

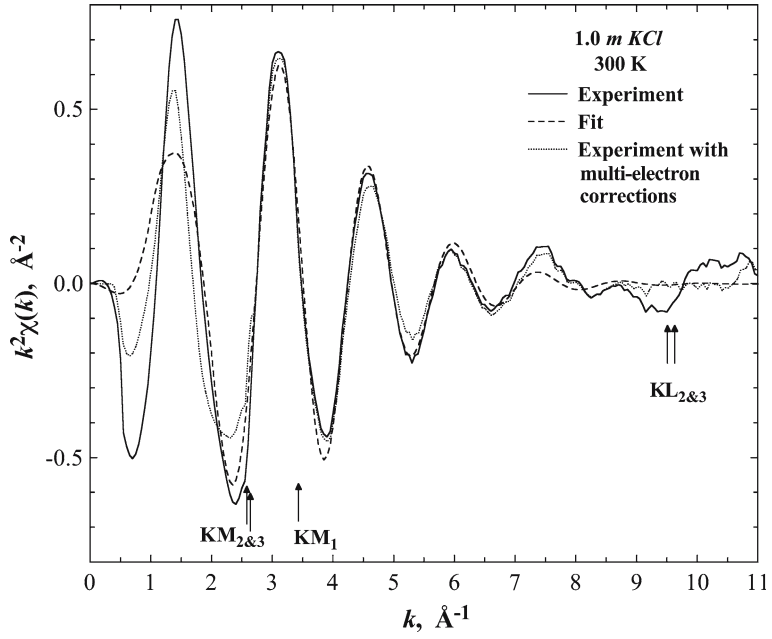


**Fig. 11** Potassium EXAFS $k^2$-weighted $\chi(k)$ plots from experiment for an aqueous 1.0 m KCl solution at 300 K. The *solid line* represents the experimental data and the *dashed line* is the theoretical fits using the parameters reported in Table 5. Also shown (*dotted line*) is the spectrum in which the multi-electron features have been removed using the procedure described in the text

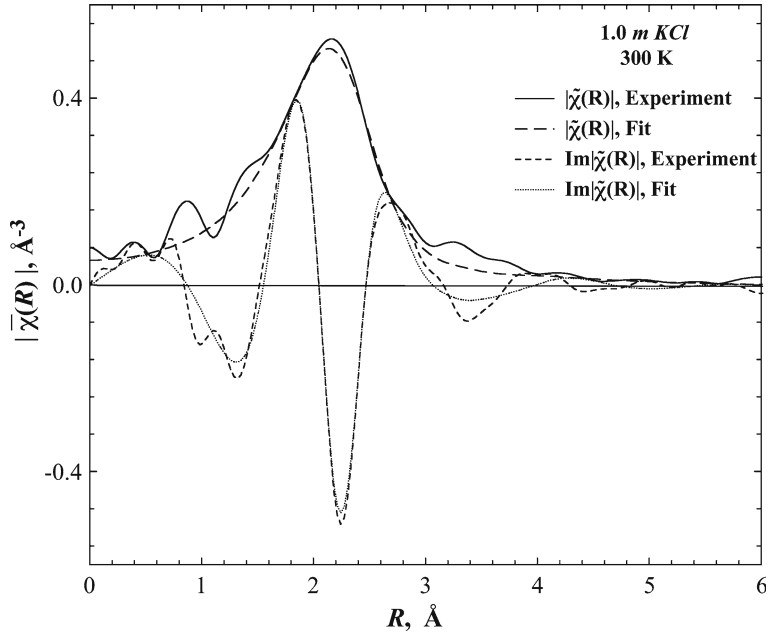


**Fig. 12** The magnitude and imaginary parts of the Fourier transforms, $k^2$-weighted $|\tilde{\chi}(R)|$ plots derived from the spectra shown in Fig. 11 for the 1.0 m KCl solution. Both the experimental data and the fits using the FEFF calculations are shown. The $|\tilde{\chi}(R)|$ plot is uncorrected for phase shifts whereas the corrected distances are reported in Table 5

number 3.5 derived from the MD-EXAFS is significantly smaller than the value of 6.8 derived from the integration of $g(r)$ to the first minimum at ∼3.5 Å (Table 2). The K–O distance derived from MD-EXAFS of 2.722 Å, is nearly equal to the value derived from the maximum in the first peak of $g(r)$ of 2.770 Å. From the two factors we can see that the EXAFS sensitivity extends considerably beyond the first peak of $g(r)$, as is shown schematically in Fig. 1, but probably does not encompass the long range tail that extends into the first minimum. Because of this effect, one would expect that the coordination number for the experimental system might be significantly higher than 6.1 when including the region of the first solvation shell out to the minimum in the $g(r)$. This larger coordination number measured experimentally may be

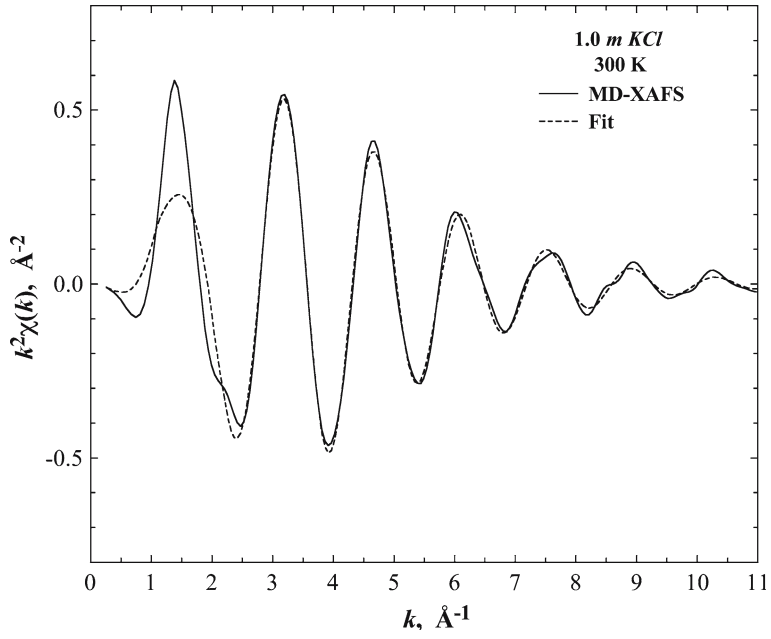


**Fig. 13** Potassium EXAFS $k^2$-weighted $\chi(k)$ plots from MD-XAFS for a 1.0 m KCl solution at 300 K. The *solid line* represents the MD simulation data and the *dashed line* is the theoretical fits using the parameters reported in Table 5

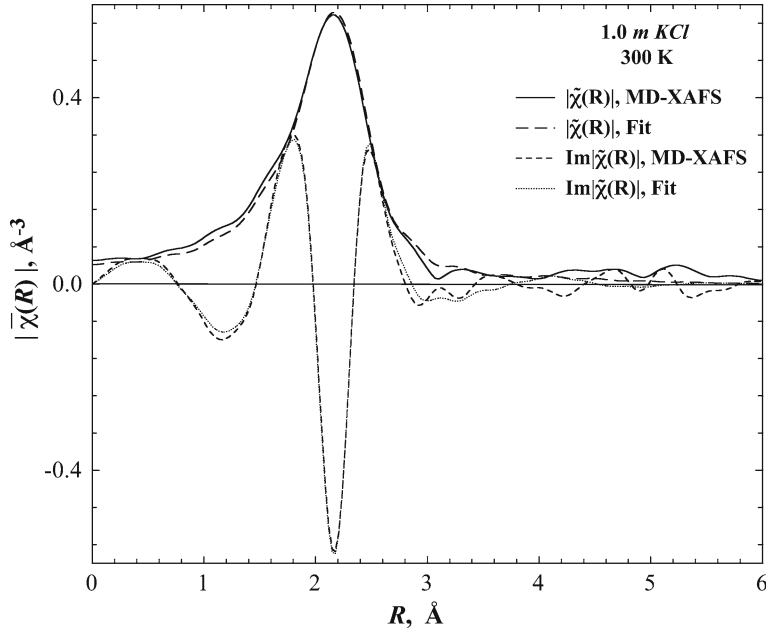


**Fig. 14** The magnitude and imaginary parts of the Fourier transforms $k^2$-weighted $|\tilde{\chi}(R)|$ plots derived from the spectra shown in Figs. 13 and 12 for the MD-XAFS simulated 1.0 m KCl solution. Both the simulated data and the fits using the FEFF calculations are shown. The $|\tilde{\chi}(R)|$ plot is uncorrected for phase shifts whereas the corrected distances are reported in Table 5

partially an artifact of the FEFF analysis. A difficulty arises in the EXAFS calculations when treating the proton on the oxygen of water. The relatively short O–H bond distances lead to a distortion of the oxygen muffin-tin potential that affects the scattering amplitudes at low-$k$, and hence the ability to estimate the coordination number. A correction for this effect has been implemented in the latest version of FEFF8 [64]. However, in the case of K–O scattering, a more demanding condition for the theory is needed, since the K–O distance is relatively large and the disorder is relatively high, imposing the need to include in the fits the low-$k$ region down to at least 2 Å$^{-1}$. In our calculations we employed the usual self-consistent potential treatment within FEFF8.20 to generate the fits leading to the parameters reported in Table 5. Exploration of more accurate treatment of the muffin tin potential is beyond the scope of this paper. It should be noted however

**Table 5** EXAFS analysis of the $K^+$ first shell structure from experimental and molecular dynamics simulations data for a 1 m KCl solution at 300 K

| Source | Method | Atom | $N$ | $R$(Å) | $\sigma^2 \times 10^3$ (Å$^2$) | $C_3 \times 10^4$ (Å$^3$) | $\mathbb{R}^{\alpha a}$ |
|---|---|---|---|---|---|---|---|
| Exp. | EXAFS[b] | O | 6.1(1.0) | 2.732(021) | 29.3(4.1) | – | 0.042 |
| MD | MD-EXAFS | O | 3.5(0.2) | 2.722(014) | 13.0(0.8) | 7.5(3.5) | 0.005 |
| MD | RDF[c] | O | 5.7 | 2.770 | 22.1 | – | – |

In all cases, the $k$-weight for the fit is 3
[a]Goodness of fit defined by a scaled sum of squares as described by FEFFIT [32]. Uncertainties in parentheses
[b]Analysis of KCl solution data with the spectrum corrected for the three multi-excitation edges
[c]From integration of a Gaussian function fit to the first peak of the radial distribution function (RDF), $g_{KO}(r)$, this work

that within the FEFF8.20, we tested a variety of different ion–water configurations, degrees of potential overlap and systems with or without the protons on the water. All these perturbations have little effect on the measured K–O distance or the Debye–Waller factor that are reported in Table 5.

## 4 Conclusions

This study combines theoretical and experimental techniques to describe and interpret the behavior of water-solvated potassium. Molecular simulations with a polarizable potential were used to calculate the RDF, local coordination and disorder at three different temperatures. *Ab initio* calculations were performed at a correlated level with augmented basis sets to locate different K-water clusters and compute the Debye–Waller factor, a measure of the disorder in the solute's immediate environment, within the harmonic approximation. These two different approaches are successfully combined in our novel approach to interface molecular dynamics with high level, electronic structure cluster calculations to obtain a theoretical, expectation value for the Debye–Waller factors. MD-simulated EXAFS spectra underestimate the Debye–Waller factor, while the ab initio-MD hybrid approach for the evaluation of EXAFS parameters, is in excellent agreement with the experimental data. Overall, the coordination number for water-solvated potassium at room temperature is $6\pm2$ and the K–O average distance $2.730\pm0.05$ Å. The Debye–Waller factor is calculated at 0.0276 Å$^2$, while the experimental value is 0.0293 Å$^2$.

**Acknowledgements** This work was supported by the Office of Science, Office of Basic Energy Sciences, Chemical Sciences Division of the U.S. Department of Energy (DOE). The Pacific Northwest National Laboratory is operated by Battelle for the DOE. PNC-CAT facilities and research at these facilities is supported by the US DOE Office of Science Grant no. DEFG03-97ER45628. Use of the Advanced Photon Source was supported by the U.S. Department of Energy, Office of Science, Office of Basic Energy Sciences, under Contract No. W-31-109-ENG-38.

## References

1. Arbman M, Siegbahn H, Pettersson L, Siegbahn P (1985) Mol Phys 54:1149–1160
2. Caldwell J, Dang LX, Kollman PA (1990) J Am Chem Soc 112:9144–9147
3. Chandrasekhar J, Spellmeyer DC, Jorgensen WL (1984) J Am Chem Soc 106:903–910
4. Cieplak P, Kollman P (1990) J Chem Phys 92:6761–6767
5. Dang LX, Rice JE, Caldwell J, Kollman PA (1991) J Am Chem Soc 113:2481–2486
6. Feller D (1997) J Phys Chem 101:2723
7. Feller D, Glendening ED, Kendall RA, Peterson KA (1994) J Chem Phys 100:4981–4997
8. Feller D, Glendening ED, Woon DE, Feyereisen MW (1995) J Chem Phys 103:3526–3542
9. Glendening ED, Feller D (1996) J Phys Chem 100:4790–4797
10. Kistenmacher H, Popkie H, Clementi E (1974) J Chem Phys 61:799–815
11. Baik J, Kim J, Majumdar D, Kim KS (1999) J Chem Phys 110:9116–9127
12. Marcus Y (1985) Ion solvation, Wiley, New York
13. Dzidic I, Kebarle P (1970) J Phys Chem 74:1466
14. Tang IN, Castleman AW (1972) J Chem Phys 57:3638
15. Haag WR, Yao CCD (1992) Environ Sci Technol 26:1005–1013
16. Chazin WJ (1995) Nat Struct Biol 2:707–710
17. Impey RW, Madden PA, McDonald IR (1983) J Phys Chem 87:5071–5083
18. Ohtaki H, Radnai T (1993) Chem Rev 93:1157–1204
19. Doyle DA, Cabral JM, Pfuetzner RA, Kuo AL, Gulbis JM, Cohen SL, Chait BT, MacKinnon R (1998) Science 280:69–77
20. Allen MP, Tildesley DJ (1987) Computer simulation of liquids, Clarendon Press, Oxford
21. Rick SW, Stuart SJ, Berne BJ (1994) J Chem Phys 101:6141–6156
22. Dang LX, Chang TM (1997) J Chem Phys 106:8149–8159
23. Chang TM, Dang LX (1999) J Phys Chem B 103:4714–4720
24. Bock CW, Glusker JP (1993) Inorg Chem 32:1242–1250
25. Bock CW, Katz AK, Glusker JP (1995) J Am Chem Soc 117:3754–3763
26. Katz AK, Glusker JP, Beebe SA, Bock CW (1996) J Am Chem Soc 118:5752–5763
27. Åkesson R, Pettersson LGM, Sandstrom M, Wahlgren U (1994) J Am Chem Soc 116:8691–8704
28. Neilson GW, Mason PE, Ramos S, Sullivan D (2001) Phil Trans R Soc London, Ser A Math Phys Eng Sci 359:1575–1591
29. Neilson GW, Skipper N (1985) Chem Phys Lett 114:35–38
30. Enderby JE (1995) Chem Soc Rev 24:159–168
31. Koningsberger DC, Prins R (1988) X-Ray absorption: principles, applications, techniques of EXAFS, SEXAFS and XANES, Wiley, New York
32. Newville M, Ravel B, Haskel D, Rehr JJ, Stern EA, Yacoby Y (1995) Physica B 209:154–156
33. Stöhr J (2003) NEXAFS spectroscopy, Springer, Berlin Heidelberg New York
34. Filipponi A (2001) J Phys Condens Matter 13:R23–R60
35. Ferlat G, Soetens JC, San Miguel A, Bopp PA (2005) J Phys Condens Matter 17:S145–S57
36. Ankudinov AL, Bouldin CE, Rehr JJ, Sims J, Hung H (2002) Phys Rev B 65:104107
37. Dang LX, Schenter GK, Fulton JL (2003) J Phys Chem B 107:14119–14123
38. Palmer BJ, Pfund DM, Fulton JL (1996) J Phys Chem 100:13393–13398

39. Berendsen HJC, Postma JPM, Vangunsteren WF, Dinola A, Haak JR (1984) J Chem Phys 81:3684–3690
40. Rehr JJ, Albers RC, Zabinsky SI (1992) Phys Rev Lett 69:3397–3400
41. Marcos ES, Martinez JM, Pappalardo RR (1996) J Chem Phys 105:5968–5970
42. Markham GD, Glusker JP, Bock CL, Trachtman M, Bock CW (1996) J Phys Chem 100:3488–3497
43. Lee HM, Kim J, Lee S, Mhin BJ, Kim KS (1999) J Chem Phys 111:3995–4004
44. Laidig KE, Speers P, Streitwieser A (2000) Coord Chem Rev 197:125–139
45. Pavlov M, Siegbahn PEM, Sandstrom M (1998) J Phys Chem A 102:219–228
46. Kaupp M, Schleyer PV (1992) J Phys Chem 96:7316–7323
47. Bauschlicher CW, Langhoff SR, Partridge H, Rice JE, Komornicki A (1991) J Chem Phys 95:5142–5148
48. Marcus Y (1988) Chem Rev 88:1475–1498
49. Dunning TH (1989) J Chem Phys 90:1007–1023
50. Woon DE, Dunning TH (1995) J Chem Phys 103:4572–4585
51. Schafer A, Horn H, Ahlrichs R (1992) J Chem Phys 97:2571–2577
52. Schmidt MW, Baldridge KK, Boatz JA, Elbert ST, Gordon MS, Jensen JH, Koseki S, Matsunaga N, Nguyen KA, Su SJ, Windus TL, Dupuis M, Montgomery JA (1993) J Comp Chem 14:1347–1363
53. Johnson RDE (2005) CCCBDB: NIST computational chemistry comparison and benchmark database, NIST standard reference database
54. Fulton JL, Heald SM, Badyal YS, Simonson JM (2003) J Phys Chem 107:4688–4696
55. Frenkel AI, Stern EA, Qian M, Newville M (1993) Phys Rev B 48:12449–12458
56. D'Angelo PD, Nolting H-F, Pavel NV (1996) Phys Rev A 53:798–805
57. D'Angelo P, Di Cicco A, Filipponi A, Pavel NV (1993) Phys Rev A 47:2055–2063
58. Filipponi A (1995) Physica B 208 & 209:29–32
59. Gomilsek JP, Kodre A, Arcon I, Preseren R (2001) Phys Rev A 64:022508
60. Zhang K, Stern EA, Rehr JJ, Ellis F (1991) Phys Rev B 44:2030–2039
61. Ramaniah LM, Bernasconi M, Parrinello M (1999) J Chem Phys 111:1587–1591
62. Rempe SB, Asthagiri D, Pratt LR (2004) Phys Chem Chem Phys 6:1966–1969
63. Fulton JL, Heald SM, Badyal YS, Simonson JM (2003) J Phys Chem A 107:4688–4696
64. Wilson KR, Tobin JG, Ankudinov AL, Rehr JJ, Saykally RJ (2000) Phys Rev Lett 85:4289–4292